Post-tilleyite, a dense calcium silicate-carbonate phase

Post-tilleyite, a dense calcium silicate-carbonate phase

David Santamaria-Perez[1,*], Javier Ruiz-Fuertes[2], Miriam Peña-Alvarez[3], Raquel Chulia-Jordan[1], Tomas Marqueño[1], Vanessa Gutiérrez-Cano[2], Simon MacLeod[4], Catalin Popescu[5], Eugene Gregoryanz[3], P. Rodriguez-Hernández[6], Alfonso Muñoz[6]

[1] MALTA-Departamento de Física Aplicada-ICMUV, Universidad de Valencia, 46100, Valencia, Spain.
[2] DCITIMAC, Universidad de Cantabria, MALTA Consolider Team, 39005, Santander, Spain.
[3] Centre for Science at Extreme Conditions and School of Physics and Astronomy, University of Edinburgh, Edinburgh EH9 3JZ, UK
[4] Atomic Weapons Establishment, Aldermaston, Reading, RG7 4PR, UK
[5] ALBA-CELLS, 08290, Cerdanyola, Spain
[6] Departamento de Física, Instituto de Materiales y Nanotecnología, Universidad de La Laguna, MALTA Consolider Team, 38206 La Laguna, Tenerife, Spain.

Abstract

Calcium carbonate is a relevant constituent of the Earth's crust that is transferred into the deep Earth through the subduction process. Its chemical interaction with calcium-rich silicates at high temperatures give rise to the formation of mixed silicate-carbonate minerals, but the structural behavior of these phases under compression is not known. Here we report the existence of two dense polymorphs of $Ca_5(Si_2O_7)(CO_3)_2$ tilleyite above 8 and 21 GPa, respectively. We have structurally characterized the first two phases at high pressures and temperatures, determined their equations of state and analyzed the evolution of the polyhedral units under compression. This has been possible thanks to the agreement between our powder and single-crystal XRD experiments, Raman spectroscopy measurements and ab-initio simulations. The presence of multiple cation sites, with variable volume and coordination number (6 – 9) and different compressibility regimes, together with observation of significant amounts of alumina in compositions of some natural tilleyite assemblages suggests that post-tilleyite structure has the potential to accommodate cations with different sizes and valencies.

With the possibility of efficient deep carbon ingassing during the last billion years of Earth's history [1], the study of the nature of stable forms of carbon in Earth's mantle and their variation as a function of depth is an important area of investigation. At convergent boundaries, carbon enters into Earth's mantle via subduction in form of carbonates [2]. Depending of the chemical environment and the thermodynamical conditions, some carbonates may survive in subducting slabs, diving deeper into the mantle [3,4]. Melting phase relations of recycled oceanic crust recently reported suggest that slabs should undergo melting and loss of carbonate components at 300-700 km depths [5]. However, the form carbon takes depends on the redox conditions in inner Earth, which is defined in terms of oxygen fugacity of the environment. The carbon oxidation state is still poorly constrained and is debated at present, but recent studies considered that carbonates may get reduced to diamond below ~250 km depth [6,7] due to a low oxygen fugacity [8]. Therefore, the structure and properties of compositionally relevant oxidized carbon-bearing phases at shallower depths (upper mantle) are of great interest for the geophysical community. In this sense, silicate-carbonates are potential host structures for carbon in Earth's interior, particularly in the proximity of carbonate-rich subduction slabs.

Only a few minerals that contain both silicate and carbonate groups exist, three of them belonging to the CaO-CO_2-SiO_2 system: $Ca_7(SiO_4)_3(CO_3)$ galuskinite [9], $Ca_5(SiO_4)_2(CO_3)$ spurrite [10], and $Ca_5(Si_2O_7)(CO_3)_2$ tilleyite [11]. They form in the metamorphic zone between limestones (sharp contact with marble, mainly composed of $CaCO_3$ calcite) and igneous rocks ($CaSiO_3$ wollastonite and other silicate minerals), at low pressures and high temperatures [12,13]. Significant aqueous fluid fluxes in marbles and calc-silicate rocks may result in the production of these types of minerals at lower temperatures, depending also on fluid composition [14]. Thermodynamical data and phase relations of minerals in this ternary system are scarce [14,15]. Liu and Lin studied the phase stability of two of these calcium silicate carbonates, spurrite and tilleyite, using laser-heated diamond-anvil cells and found that these minerals decompose into their component silicates and carbonates above 4 GPa and ~1000º C [16]. On the other hand, experimental studies at low pressures suggest that spurrite and tilleyite have a field of stability between 600º and 1000º C [12,17]. It is then fundamental to invest in a more detailed knowledge of these compounds at pressures and temperatures of deep subduction regions, since these silicate-carbonate minerals might be constituents of "cold" slabs. In this regard, it is important to attain an accurate description of the crystal structures and physical properties of these materials at high pressures and temperatures. The compressibility and phase stability of spurrite up to 27 GPa and 700 K have been recently reported [18]. No phase transformation was found, which suggests that the presence of carbonate [CO_3] units gives stability to the tetrahedral [SiO_4] orthosilicate group, holding up the

formation of phases based on octahedral [SiO_6] units. What occurs to tilleyite with a similar configuration remains unknown.

Tilleyite is a naturally-occurring calcium silicate-carbonate mineral that conforms well with the chemical formula $Ca_5(Si_2O_7)(CO_3)_2$, but some minor substitution of other elements such as Al, Mg or F could occur [12,19]. It is therefore the most carbonated compound of the calcium silicate-carbonate family. The existence of this mineral was firstly reported by Larsen and Durham in 1933 from contact altered limestones at Crestmore quarries, California, USA [11]. The monoclinic crystal structure of tilleyite was firstly determined by Smith [20] and later refined by Louisnathan and Smith [21], and Grice [22]. The structure contains the following atom-centered oxygen polyhedra as building blocks: [CO_3] triangles, [SiO_4] tetrahedra forming disilicate [Si_2O_7] units, and five irregular polyhedra with different coordination spheres for Ca atoms (20% are octahedrally coordinated, 60% are forming 7-fold-coordinated capped octahedra and 20% are forming distorted cubes). It is envisaged that the flexibility of the bridging Si – O – Si dihedral angle of the disilicate group upon compression could lead to an increase of the coordination number of the Ca atoms and the transition to a denser phase.

Here we present, in contrast to spurrite, the formation of a novel silicate-carbonate phase after compressing tilleyite above 8 GPa. The high-pressure polymorph is characterized *in situ* by X-ray diffraction (XRD) and Raman spectroscopy. DFT calculations confirm that the new phase is thermodynamically stable at these conditions. We also found evidence for a second dense silicate-carbonate polymorph above 21 GPa. The initial tilleyite structure is recovered after pressure is quenched.

Results

Phase stability and determination of a high-pressure phase

Powder and single-crystal XRD measurements on tilleyite were performed under compression. The initial sample can be described with a monoclinic $P2_1/n$ space group and lattice parameters: a = 7.582(4) Å, b = 10.265(4) Å, c = 15.030(6) Å and β = 103.99(2)º (V = 1135.0(9) Å^3, Z =4), which are in excellent agreement with previously reported cell dimensions of other Crestmore specimens (once expressed in the same crystallographic setting). The structure is depicted in Figures 1a-c and the atomic coordinates of the 22 independent atoms within the unitcell at ambient conditions are collected in Table 1 of Supplementary Information, SI (to be compared with literature data of Table 2). The topological features of the structure are the same as previously determined, but a brief summary is needed to analyze subsequent structural transformations. In tilleyite, two [SiO_4] tetrahedra share a common O atom to form a disilicate [Si_2O_7] group along the a axis and the [CO_3] carbonate units

are roughly oriented along the [001] direction. Ca polyhedra and disilicate units form corrugated walls parallel to (001) cross-linked by the [CO_3] triangles. Voronoi-Dirichlet polyhedra of Ca atoms provide reliable information on the number of atoms that must be considered as first neighbors for bonding purposes [23]. There are five Ca sites with three types of coordination: 1 x [CaO_6], 3 x [CaO_7] and 1 x [CaO_8]. Except the octahedron, the other Ca-centered polyhedra are very irregular and difficult to describe. Major distortions likely come from the shortening of edges shared between polyhedra, as expected from electrostatic interactions [21]. For instance, a result of the cooperative accommodation of the different building units is that the [Si_2O_7] groups flex to yield a dihedral angle of XXXº.

Powder diffraction data present intensities that do not correspond to perfect randomly oriented powder, so only peak positions and not relative intensities could be used to the structural analysis. In other words, from powder diffraction data, we could only accurately infer the lattice parameters of the mineral upon compression (see an example of LeBail refinement in Figure 1 of SI). Indexations and profile fittings of the powder XRD patterns up to 22 GPa, the maximum pressure reached in this study, suggest that the structure can be described by a monoclinic space group and comparable unit cell dimensions in the whole pressure range. However, the evolution of the lattice parameters (Figure 2), the monoclinic beta angle (Figure 2), and unit-cell volume (Figure 3) as a function of pressure evidence a clear discontinuity at 8-9 GPa. More specifically, according to our experiments (calculations), the *a* axis does not change noticeably, but *b* and *c* axes decrease at the transition about 0.2 (0.5) and 1.3 (1.5)%, respectively, and the *β* monoclinic angle suddenly decreases about 0.28 (0.12)º, giving as a result a unit cell contraction of about 1.5 (2.1)%. It is worth noting that the low symmetry and the large unit cell parameters preclude an unequivocal space group assignment, since numerous reflections overlap in powder XRD patterns. This problem is accentuated upon compression with the progressive broadening of the XRD reflections.

Single-crystal XRD measurements allow us to fully characterize the progressive transformations of the tilleyite structure with increasing pressure and the nature of the high-pressure silicate-carbonate phase. Our results show that in tilleyite there is a Ca – O distance that rapidly decrease upon compression, increasing the formal coordination number of one of the seven-fold coordinated Ca atoms to eight for pressures above 6 GPa (see crystallographic data of tilleyite at 7.9 GPa in Table 3 of SI). Above 9 GPa, the crystal structure can not longer be described by the tilleyite $P2_1/n$ space group, but by the lower symmetry $P2_1$ space group. The structure was solved with a dataset at 10.8 GPa that has a reciprocal space completeness of 26.7 % up to a resolution of 0.46 Å. The position of the Ca and Si atoms was determined by SHELXT [24]. Subsequent structural refinement and analysis of the difference-Fourier maps of the electron

density function afforded localizing the rest of atoms of the unitcell. The final refinement of the structure was performed with SHELXL [25] and included all the atomic coordinates and the isotropic displacement parameters. Data pertinent to the intensity data collection are given in Table 1 and the final positional parameters of post-tilleyite at 10.8 GPa are collected in Table 2.

Figures 1d-f show the projections of the high-pressure phase, hereafter named post-tilleyite, along the crystallographic axes. Although the transition comes with a volume collapse of ~1.5%, the symmetry of the initial and final structures is related by a group-subgroup relationship and they can be easily compared (see Figures 1a-f). The coordination spheres around the C and Si atoms by O atoms have not changed, remaining in trigonal planar and tetrahedral configuration. However, in contrast to tilleyite, the [CO_3] groups in post-tilleyite are no longer coplanar with each other. Half of them maintain their initial orientation whereas ¼ are now roughly perpendicular to the *c* axis and ¼ are roughly perpendicular to the *a* axis. A similar rotation of carbonate groups was observed in the high-pressure polymorph of calcite, $CaCO_3$-III [26]. This fact supports previous descriptions of tilleyite in terms of silicate and carbonate separated layer modules, where the $CaCO_3$ component seems to follow a crystal behavior comparable to that of calcite itself in the same pressure range ($CaCO_3$-III is reported to be stable between 2.5 and 15 GPa).

Post-tilleyite also contains two types of disilicate groups due to symmetry reduction, which causes that the Wyckoff positions 4e in the tilleyite $P2_1/n$ structure split into two symmetrically independent 2a positions. The dihedral angle of the [Si_2O_7] units change at the transition from 154.3º at 7.9 GPa to 149.4º and 156.7º at 10.8 GPa. These topological transformations entail considerable changes in the coordination number of Ca atoms. For instance, at 10.8 GPa, analyses of Voronoi-Dirichlet polyhedra reveal that Ca – O distances between 2.16 and 2.88 Å make up the Ca first-coordination spheres in post-tilleyite, defining variable Ca coordination polyhedra in different sites. The Ca coordination number varies from 6 to 9 (1 x [CaO_6], 3 x [CaO_7], 5 x [CaO_8], 1 x [CaO_9]). The existence of such a range of different polyhedral volumes within the same structure is very unusual and interesting from the geophysical point of view. Such a structure could likely host divalent cations with different radii without inducing significant elastic strains. This is particularly relevant within the complex scenario of Earth's mantle, where natural compositions likely include Mg^{2+}, Fe^{2+}, and other cations coexisting with Ca^{2+}. Thus, post-tilleyite offers a versatile structural possibility in comparison with aragonite, the most stable structure for Ca-rich carbonates in the upper and intermediate mantle, which has large polyhedral voids to host small cations (Ca atoms in nine-fold coordination).

To further understand the structural evolution of tilleyite under compression, we performed *in situ* Raman spectroscopy measurements up to 25 GPa. Group

theoretical analyses (point group C_{2h}) predict 132 Raman active modes Γ_R = $66A_g$ + $66B_g$) and a complicated Raman spectrum [27]. Raman scattering spectra at some representative pressures are shown in Figure 4. The large number of modes of low-pressure $Ca_5(Si_2O_7)(CO_3)_2$ tilleyite precludes mode identification and only a rough assignment of fundamental vibrational modes was done. They can be distributed according to the following grouping: librational modes involving Ca^{2+} and [SiO_4] and [CO_3] units below 400 cm^{-1}; bending modes of [SiO_4] and [CO_3] units between 400 and 780 cm^{-1}; internal stretching of the [SiO_4] and [CO_3] groups in the 800-1500 cm^{-1} range, and OH stretching region above 2800 cm^{-1}.

The most intense bands appear between 900 and 1100 cm^{-1}. The band at 905 cm^{-1} corresponds to the Si-O stretching of the tetrahedral units [28]. The intense triplet between 1083 and 1093 cm^{-1} corresponds to the symmetric C-O stretching from the [CO_3] units. The triplet structure is a consequence of the different environment surrounding the two distinct non-equivalent [CO_3] units of tilleyite. In the lower frequency region, at 649 cm^{-1}, the bending of the Si-O-Si inter-tetrahedral linkage appears [29-31]. The bands between 697 and 780 cm^{-1} are assigned to the [CO_3] bending mode. In the low frequency region, the broad band at around 300 cm^{-1} is likely related to Ca-O connections, in analogy with the assignment done for wollastonite [31]. On the higher frequency region at around 1500 cm^{-1} the antisymmetric C-O stretching mode appears. Moreover, at around 3500 and 3700 cm^{-1}, we observe two broad bands corresponding to O-H stretching mode of water and intersticial OH [27]. Due to the low intensity of these OH modes they were not always detected.

In Figure 4 it can be seen the general upshift of the bands of tilleyite with increasing pressure (see also Figure 2 of Supplementary Material). No significant broadening is observed as expected by the crystallinity of the solid and the hydrostaticity provided by the pressure transmitting medium. In the low frequency region there are changes in the relative intensities of the modes that could be explained by the continuous change towards a higher coordination number of the Ca atoms induced by pressure, as revealed in XRD experiments.

Interestingly, between 8-9 GPa there is an abrupt splitting of the Si-O band and an even more remarkable one of the C-O bands, which perfectly agree with XRD results of the tilleyite to post-tilleyite transition. The orientational change of the [CO_3] groups explains the splitting of the C-O stretching as its environment has changed. The splitting of the Si-O stretching into two contributions is perfectly explained by existence of two types of unequivalent disilicate groups [Si_2O_7] in post-tilleyite while in tilleyite there was only one. In the bending mode regions between 600 and 800 cm^{-1}, the Si-O bending splits into several contributions and some of them blueshifts as a consequence of the observed decrease in the Si-O-Si bond angle [30]. On the other hand, the prints from the lattice modes drastically change as there appears an intense band at around 80

cm^{-1}. The splitting of all the contributions at the phase transition is illustrated in Figure 2 of the Supplementary Material. Moreover, there is a change in the O-H stretching region at the transition as a new contribution appears at around 3000 cm^{-1}. The presence of O-H stretching and bending bands provides evidence for the existence of $[SiO_3(OH)]$ groups in both, the low- and high-pressure phases. In addition to that aforementioned, the spectroscopic results presented in Figure 4 suggest an additional structural transition between 19 and 25 GPa, as inferred from the disappearance of sharp peaks and the appearance of very broad bands change in the spectrum profile. Pressure-induced amorphization was ruled out because post-tilleyite and tilleyite spectra were observed on pressure release.

Theoretical DFT calculations confirm that post-tilleyite is the thermodynamically stable structure at high-pressures. Figure 5 shows the energy as a function of volume curves for the initial tilleyite and high-pressure post-tilleyite calculated structures. It can be clearly seen that both curves cross each other at high pressure. As shown in the enthalpy as a function of pressure graph of Fig. 5 inset, the denser phase becomes more stable at 8 GPa, in excellent agreement with the experimental data. Structural data from DFT calculations are also collected in Supplementary Material. Our simulations also provide frequencies and pressure coefficients of the IR- and Raman-active optical vibrations and, interestingly, show that some low-frequency modes corresponding to the tilleyite phase become softer with increasing pressure and eventually vanish at the phase transition pressure (Figure 3 of Supplementary Material). Furthermore, our theoretical data predict that post-tilleyite will be dynamically unstable above 21 GPa (Figure 4 of Supplementary Material), which supports the existence of the second pressure-induced phase transition observed in Raman experiments.

Figures 2 and 3 illustrate the compression dependence of the lattice parameters and unit-cell volumes of both, tilleyite and post-tilleyite phases. The experimental and theoretical values are in good agreement and show a smooth and monotonous decrease under pressure. The strong anisotropy of tilleyite is described by the approximate linear axial compressibility values: $\beta_a = 2.84(3)\cdot10^{-3}$, $\beta_b = 3.79(8)\cdot10^{-3}$ and $\beta_c = 3.48(9)\cdot10^{-3}$ GPa^{-1} for the *a*, *b*, and *c* axes, respectively. These experimental axial compressibilities agree well with theoretical results: $\beta_a = 2.8(1)\cdot10^{-3}$, $\beta_b = 3.92(5)\cdot10^{-3}$ and $\beta_c = 4.00(6)\cdot10^{-3}$ GPa^{-1}. Whereas the *b* and *c* lattice parameters show a quite similar relative contractions, the *a* axis is prominently harder (large incompressibility and rigidity of the $[Si_2O_7]$ disilicate units), which means that the bulk compressibility will be dominated by that of the *b* and *c* axes. The least-squares fit of a second-order Birch−Murnaghan equation of state (BM-EoS) [32] to our experimental (theoretical) pressure-volume data of the initial phase give a zero-pressure unitcell volume, $V_0 = 1131(1)$ $Å^3$ (1119.5(6) $Å^3$) and a bulk modulus, $B_0 = 80(2)$ GPa (75.3(4) GPa). These values reflect a slightly higher compressibility than

those reported by Gao and coworkers: V_0 = 1168.90(2) Å^3, B_0 = 69.7(3) GPa, and B'_0 = 4.0(1) from DFT calculations using the PBE prescription [33]. Post-tilleyite is only slightly more incompressible with BM-EoS characteristic parameters: V_0 = 1110(4) Å^3 (1088.7(4) Å^3) and B_0 = 83(3) GPa (82.1 (3) GPa), according to experimental (theoretical) results. Linear axial compressibilities indicate that the high-pressure phase is more isotropic: β_a = 2.3(2)·10^{-3} GPa^{-1} (2.64(3)·10^{-3} GPa^{-1}), β_b = 2.5(2)·10^{-3} GPa^{-1} (2.31(5)·10^{-3} GPa^{-1}) and β_c = 2.2(1)·10^{-3} GPa^{-1} (2.00(4)·10^{-3} GPa^{-1}) for the *a*, *b*, and *c* axes, respectively.

The evolution of the polyhedral units with compression is shown in Fig. 6. The compression of the unit cell is dominated by the compression of the softer calcium-centered polyhedral units. In the case of the low-pressure tilleyite phase, two types of polyhedra have a lower bulk modulus than the unit cell, a seven-fold [CaO_7] capped-octahedron and the [CaO_6] octahedron, with $B_{0(P1)}$ = 54.6(9) and $B_{0(P2)}$ = 66.2(6) GPa, respectively. After the transition, the remaining [CaO_6] octahedron exhibits a similar compressibility $B_{0(P3)}$ = 89.0(9) GPa to that of the unitcell, but two other polyhedral units are more compressible under compression: an 8-fold and the 9-fold coordinated Ca units with 62.7(3) and 83(1) GPa, respectively. Note that the diversity of environments of the Ca atoms is not only defined by the number of oxygen neighbours but also by the range of compressibilities of the different [CaO_n] polyhedra, with bulk moduli as high as 139 (3) GPa.

Tilleyite was also studied at high-pressure high-temperature. The sample was progressively compressed and heated up to 7.2 GPa and 675 K while characterized collecting *in situ* powder XRD data. The HP-HT patterns were indexed using the isolated single reflections and confirmed that the tilleyite structure remained stable in that P-T range. Due to the fact that the pressure is not constant during heating, we used a perturbational method to estimate the thermal expansivity at low pressures, as described in Ref. 18. This approximation has been successfully used to calculate the thermal expansivity under compression in other compounds [34,35]. A linear fit to our data yields a volumetric thermal expansion value of 3.5(4)·10^{-5} K^{-1}. The thermal expansivity of tilleyite lies between those of $CaCO_3$ aragonite (6.53·10^{-5} K^{-1}) and $CaCO_3$ calcite (2.01·10^{-5} K^{-1}) [36], and it is similar to those of calcium silicate β-Ca_2SiO_4 larnite (4.24(4)·10^{-5} K^{-1}) [37] at room pressure and $Ca_5(SiO_4)_2(CO_3)$ spurrite at ~8 GPa (4.1(3)·10^{-5} K^{-1}) [18]. $CaSiO_3$ wollastonite, another end-member calcium silicate, exhibits a smaller thermal expansion (5.7-7·10^{-6} K^{-1}) [38]. This fact suggests therefore that the thermal expansivity of $Ca_5(Si_2O_7)(CO_3)_2$ tilleyite (2 $CaCO_3$ + Ca_2SiO_4 + $CaSiO_3$ stoichiometric content) is a consequence of the structural homologies in the atomic arrangements with other members of the Ca-Si-C-O system.

Discussion

The present study using a combination of powder and single-crystal XRD, Raman spectroscopy and DFT calculations clearly shows the existence of a novel silicate-carbonate polymorph under high P-T conditions. At 8 GPa, tilleyite, a naturally-occurring silicate-carbonate mineral transforms into a denser phase which presents a large variety of environments for Ca atoms, from six-fold to nine-fold coordination. The different classes of irregular cation-centered oxygen polyhedra exhibit a wide range of compressional characteristics, which suggest that such an structure could accommodate other divalent cation species with different radii ; *i.e*. Mg^{2+}, Fe^{2+}, Mn^{2+}, etc.... On top of that, systematic studies on tilleyite reveal that traces of alumina and fluoride favor its formation, in agreement with compositions of natural mineral assemblages [12]. Synthetic tilleyite has been grown from starting material with up to 8.2 and 4.7% of Al_2O_3 and CaF_2, respectively. This means that partial substitution of Si by Al atoms is possible and alkali metals of different sizes can also be hosted in both tilleyite and post-tilleyite structures. Our Raman data also shows the replacement of some oxygen atoms by OH groups. Note that potential chemical substitutions and the low symmetry of the post-tilleyite structure are envisaged to further stabilize this phase at high temperature via an increase of the entropic term.

Carbonated mantle rocks like carbonatite and kimberlite are composed of many phases, e.g.: silicates, carbonates and/or oxides, and the knowledge of these structures will help us to understand the pathways of carbon cycle in the mantle. The thermodynamic conditions for formation and preservation of $Ca_5(Si_2O_7)(CO_3)_2$ tilleyite are under debate, but it seems to be stable within the 450º [17] – 970º C [12] temperature range at low pressures (<2 Kbar). At 40 Kbar, tilleyite is reported to break down at 1000º C into a mixture of calcium carbonate and silicate phases: aragonite, wollastonite and larnite [16]. Studies on chemical reactions occurring in phase equilibrium experiments of more complex mantle representative stoichiometries at higher pressures are scarce and are basically limited to carbonatite melt temperatures [39-42]. Accurate phase relation constraints at lower temperatures (T<1000º C) are required to evaluate the possibility of tilleyite and post-tilleyite as carbon host phases in the Earth's mantle. Considering possible geological settings, Ca-enriched low-temperature subduction zones are the most likely environments where this structure could be encountered. Silicates mixed with carbonates should not exist on Earth, may exist on more massive planets.

Methods

Initial samples. Naturally occurring tilleyite crystals from the Crestmore quarry in the Jurupa mountains (Riverside County, California, USA) were kindly provided by the Yale Peabody Museum (Specimen YPM MIN 041104). A few

crystals were optically selected crystals under the microscope and crushed with a mortar and pestle, giving a fine white powder without lustre. Qualitative chemical analyses were done on a Philips XL30 scanning electron microscope by the method of energy dispersive x-ray spectroscopy. Only traces (<1 wt%) of Al and K were found apart the Ca, Si, C and O atoms present in the ideal $Ca_5(Si_2O_7)(CO_3)_2$ formulae. This is in good agreement with tilleyite chemistry reported in Ref.[11] for a tilleyite specimen collected in the same area. Angle-dispersive x-ray diffraction measurements at ambient conditions confirm the tilleyite structure.

High-pressure methods. We performed high pressure (HP) experiments at both, room (RT) and high temperature (HT) conditions and the sample was characterized *in situ* by means of synchrotron angle-dispersive x-ray diffraction measurements. HP-RT experiments to 23 GPa were carried out in a gas-membrane-driven diamond-anvil cell (DAC) equipped with diamonds of 350 μm of culet diameter. The tilleyite sample was placed together with two ruby chips at the center of a 100 μm diameter 40 μm thick pressure chamber drilled in a preindented rhenium gasket. High-purity Ne gas was also loaded in the DAC at room temperature using the Sanchez Technologies gas loading apparatus. Ne is fluid up to 4.7 GPa and acted as a quasi-hydrostatic medium in the pressure range of the study [43,44]. Pressure was determined using the ruby fluorescence method [45], which provided pressure accuracies of 0.1 GPa below 14 GPa and 0.2 GPa up to 23 GPa. The equation of state of Ne was used as a second pressure gauge [46] above 5 GPa.

High-temperature methods. For the HP resistive-heating studies, the DAC was contained within a custom-built vacuum vessel designed for HP–HT experiments [46]. The DACs were heated using Watlow 240V (rated at 4.65W cm^{-2}) coiled heaters wrapped around the outside of the DACs. The temperature was measured using a K-type thermocouple attached to one of the diamond anvils, close to the gasket. The accuracy of the thermocouple on the temperature range covered by the experiments is 0.4% [34,35]. NaCl powder was included in the sample chamber to act as pressure marker [48].

Powder XRD methods. In situ HP-RT angle-dispersive powder X-ray diffraction measurements were carried out at MSPD beamline at ALBA-CELLS synchrotron using a x-ray wavelength of 0.534 Å (Rh K edge) [49]. This beamline provides a X-ray beam focused down to ~20x20 μm^2, and the diffracted signal was collected with a Rayonix CCD detector. The detector parameters were calibrated with LaB_6 powder standard, and integration to conventional 2θ-intensity data was carried out with the Dioptas software [50]. The indexing and refinement of the powder patterns were performed using the Chekcell [51], Unitcell [52] and Powdercell [53] program packages.

Single crystal XRD (SXRD) methods. Experiments were performed with a Boehler-Almax diamond anvil cell (DAC) (4θ ~ 70º) in which a 10-μm-thick

sample was introduced inside a 150 μm diameter hole of a stainless-steel gasket preindented to 40 μm. The pressure calibrant was a ruby chip and the pressure transmitting media were Ne and a 4:1 methanol:ethanol mixture. These experiments were done at the MSPD beamline at ALBA-CELLS synchrotron using a x-ray wavelength of 0.3185 Å and at the P02.2 Extreme conditions beamline at PETRA III synchrotron, DESY, using a x-ray wavelength of 0.28973 Å. Only SXRD data mesured at PETRA III allowed the full structural refinement. The diffraction images were collected by 0.2º ω scanning. The image format was converted for further processing with the CRYSALIS*Pro* software [54] for indexing reflections and intensity data reduction. The structures were refined with SHELXL [25], operated using the WinGX interface [55].

Raman spectroscopy methods. A symmetric screw driven diamond anvil cell was used. Ultra low-fluorescent diamond anvils, with a culet diameters of 200 μm were used. Re-foil gasket was used to hold the samples, with gasket chambers of about 75 μm diameter and 30 μm thick. The hole of the chamber was laser-milled. Powdered sample was loaded in the chamber together with a ruby chip whose fluorescence is used as pressure calibrant. Argon gas was loaded into diamond anvil cells at a pressure of 0.2 GPa as pressure transmitting medium up to 9 GPa (Tateiwa N., (2009) Rev. Sci. Inst). At pressures above this hydrostaticity is not guaranteed, however it should be provided by the sample powedered itself.. High-quality Raman spectra were acquired using a custom-built micro-focused Raman system, using a 514 nm Argon laser as the excitation line. Raman scattering radiation was collected in back–scattering configuration. The device is equipped with a 20x Mitutoyo long working distance objective and focused onto the slit of a Princeton monochromator with a grating of 1800 grooves mm^{-1} and a CCD detector (1340−400 pixels). Spectra were measured with a spectral resolution of about 1−2 cm^{-1} and calibrated with a standard neon emission lamp. The DAC is mounted on a xyz stage, which allows to move the sample with an accuracy of 1 μm. The typical sampling area was about 1−2 μm in diameter.

Computational methods. The present study was performed through total energy ab initio simulations with the Vienna ab initio simulation package (VASP) plane-wave pseudopotential program [56-58]. We have employed the Born-Oppenheimer approximation and the electrons were quantum-mechanical treated by solving the Khon-Sham equations of density functional theory (DFT) [59]. The exchange-correlation energy was described with the generalized gradient approximation (GGA) approximation, according to the Perdew-Burke-Ernzerhof for solids (PBEsol) [60] prescription. The projector augmented wave (PAW) [61,62] was used to take into account the electron-ion interactions, and the plane waves basis set was extended up to a cutoff energy of 530 eV in

order to obtain accurate results. The Brillouin zone integrations were carried out by means of a grid of Monkhorst-Pack [63] (4x2x2) k-special points that provided well converged results due to the large size of the primitive cell, that contains 88 atoms, with a great number of degrees of freedom. For a set of different volumes, we achieved a total relaxation of all these free degrees to obtain the optimized structural parameter. The total energy was converged to 0.001 eV, the Hellman-Feynman forces on the atoms were lower than 0.004 eV/Å, and hydrostatic conditions were obtained, it mean that the stress tensor was diagonal with an accuracy of 0.1 GPa. After these simulations for the set of volume-fixed cells, we got the volumes, total energies and pressures, as well as the cell parameters and the Wickoff positions of the atoms. This allowed using an equation of state, EOS, to fit the data and to obtain the bulk modulus and its derivatives. This method was applied with very good results to the study of phase stability of many semiconductors compounds under high pressure [64].

References

[1] R. Dasgupta (2013) Ingassing, storage, and outgassing of terrestrial carbon through geologic time. Rev. Mineral. Geochem. 75, 183.

[2] R. Dasgupta, M.M. Hirchmann (2010) The deep carbon cycle and melting in Earth's interior. Earth Planet. Sci. Lett. 298, 1.

[3] S. Poli, E. Franzolin, P. Fumagalli, A. Crottini (2009) The transport of carbon and hydrogen in subducted oceanic crust: An experimental study to 5 GPa. Earth Planet. Sci. Lett. 278, 350.

[4] J.A.D. Connolly (2005) Computation of phase equilibria by linear programming: A tool for geodynamic modelling and its application to subduction zone decarbonation. Earth Planet. Sci. Lett. 236, 524.

[5] A.R. Thomson, M.J. Walter, S.C. Kohn, R.A. Brooker (2016) Slab melting as a barrier to deep carbon subduction. Nature 529, 76

[6] A. Rohrbach, M.W. Schmidt (2011) Redox freezing and melting in the Earth's deep mantle resulting from carbon-iron redox coupling. Nature 339, 456.

[7] V. Stagno, D.O. Ojwang, C.A. McCammon, D.J. Frost (2013) The oxidation state of the mantle and the extraction of carbon from Earth's interior. Nature 493, 84.

[8] D.J. Frost, C.A. McCammon (2008) The redox state of the Earth's mantle. Ann. Rev. Earth Planet. Sci. 36, 389.

[9] B. Lazic, T. Armbruster, V.B. Savelyeva, A.E. Zadov, N.N. Pertsev, P. Dzierzanowski (2011) Galuskinite, Ca7(SiO4)3(CO3), a new skarn mineral from the

Birkhin gabbro massif, Eastern Siberia, Russia. Mineralogical Magazine, 75, 2631-2648.

[10] Spurr, J.E.; Garrey, G.H. Ore-deposits of the Velardeña district, Mexico. *Economic Geology*, **1908**, *3*, 688-725.

[11] Larsen, E.S.; Dunham, K.C. Tilleyite, a new mineral from the contact zone at Crestmore, California. *Amer. Mineral.* **1933**, *18*, 469-473.

[12] Harker, I. The synthesis and stability of tilleyite, $Ca_5Si_2O_7(CO_3)_2$. *Amer. J. Sci.* **1959**, *257*, 656-667.

[13] Rubenach, M.J.; Cuff, C. The occurrence of coarse-grained massive tilleyite in the Redcap Creek magmatic skarn, North Queensland. *Mineral. Magaz.* **1985**, *49*, 71-75.

[14] R.J. Tracy, B.R. Frost (2019) Phase equilibria and thermobarometry of calcareous, ultramafic and mafic rocks, and iron formations. Rev. Mineral. 26, 207-289.

[15] Treiman, A.H.; Essene, E.J. Phase equilibria in the system $CaO\text{-}SiO_2\text{-}CO_2$. *Amer. J. Sci.* **1983**, *283-A*, 97-120.

[16] L-G. Liu, C-C. Lin (1995) High-pressure phase transformations of carbonates in the system CaO-MgO-SiO2-CO2. Earth Planet. Sci. Lett. 134, 297-305.

[17] C. Henmi, K. Henmi (1978) Synthesis of spurrite and tilleyite at low CO2 partial pressure. Mineralogical Journal, 9, 106-110.

[18] Santamaria-Perez, D.; Ruiz-Fuertes, J.; Marqueño, T.; Pellicer-Porres, J.; Chulia-Jordan, R.; MacLeod, S.; Popescu, C. Structural behavior of natural silicate-carbonate spurrite mineral, Ca5(SiO4)2(CO3), under high-pressure high-temperature conditions. *Inorg. Chem*. **2018**, *57*, 98-104.

[19] Anthony, J.W.; Bideaux, R.A.; Bladh, K.W.; Nichols, M.C. Eds., Handbook of Mineralogy, Mineralogical Society of America, Chantilly, VA 20151-1110, USA. http://www.handbookofmineralogy.org/.

[20] Smith, J.V. The crystal structure of tilleyite. *Acta Cryst.* **1953**, *6*, 9-18.

[21] Louisnathan, S.J.; Smith, J.V. Crystal structure of tilleyite: Refinement and coordination. *Zeits. Kristallogr.* **1970**, *132*, 288-306.

[22] Grice, J.D. The structure of spurrite, tileyite and scawtite, and relationships to other silicate-carbonate minerals. *Can. Mineral.* **2005**, *43*, 1489-1500.

[23] V.A. Blatov. Voronoi-Dirichlet polyhedral in crystal chemistry: theory and applications. *Crystal. Rev*. **2004**, *10*, 249-318.

[24] G. M. Sheldrick. SHELXT - Integrated space-group and crystal-structure determination. *Acta Cryst. A*, **2015**, *71*, 3-8.

[25] G. M. Sheldrick. Crystal structure refinement with SHELXL, Acta Cryst. C **2015**, *71*, 3-8

[26] M. Merlini, M. Hanfland, W.A. Crichton. CaCO3-III and CaCO3-IV, high-pressure polymorphs of calcite: Possible host structures for carbon in the Earth's mantle. *Earth Planet. Sci. Lett*. **2012**, *333-334*, 265-271.

[27] R.L. Frost, A. Lopez, R. Scholz, F.A.N. de Oliveira. Scanning electron microscopy with energy dispersive spectroscopy and Raman and infrared spectroscopy study of tilleyite Ca5Si2O7(CO3)2-Y. *Spectrochim. Acta A*, **2015**, *149*, 333-337.

[28] D. Santamaria-Perez, A. Thomson, A. Segura, J. Pellicer-Porres, F.J. Manjon, F. Cora, K. McColl, M. Wilson, D. Dobson, P.F. McMillan. Metastable structural transformations and pressure-induced amorphization in natural (Mg,Fe)2SiO4 olivine under static compression: A Raman spectroscopic study. *Amer. Mineral.* **2016**, *101*, 1642-1650.

[29] Y. Iguchi, S. Kashio, T. Goto, Y. Nishina, T. Fuwa. Raman spectroscopic study on the structure of silicate slags. *Can. Metall. Q.* **1981**, 20, 51-56.

[30] J.D. Kubicky, R.J. Hemley, A.M. Hofmeister. Raman and infrared study of pressure-induced structural changes in MgSiO3, CaMgSi2O6 and CaSiO3 glasses. *Am. Mineral.* **1992**, *77*, 258-269.

[31] G.C. Serghiou, W. S. Hammack. Pressure-induced amorphization of wollastonite CaSiO3 at room temperature. *J. Chem. Phys*. **1993**, *88*, 9831-9834.

[32] F. Birch. Finite elastic strain of cubic crystals. *Phys. Rev*. **1947**, *71*, 809-824.

[33] J. Gao, X. Wu, S. Qin. The crystal chemistry and the compressibility of silicate-carbonate minerals: Spurrite, galuskinite and tilleyite. *Geoscience Frontiers*, **2015**, *6*, 771-777.

[34] Santamaria-Perez, D.; Marqueño, T.; MacLeod, S.; Ruiz-Fuertes, J.; Daisenberger, D.; Chulia-Jordan, R.; Errandonea, D.; Jorda, J.L.; Rey, F.; McGuire, C.; Mahkluf, A.; Kavner, A.; Popescu, C. Structural evolution of the CO2-filled pure silica LTA zeolite under high-pressure high-temperature conditions. *Chem. Mater*. **2017**, *29*, 4502-4510.

[35] T. Marqueño, D. Santamaria-Perez, J. Ruiz-Fuertes, R. Chulia-Jordan, J.L. Jorda, F. Rey, C. McGuire, A. Kavner, S. MacLeod, D. Daisenberger, C. Popescu, P. Rodriguez-Hernandez, A. Muñoz. An ultrahigh CO2-loaded silicalite zeolite: Structural stability and physical properties at high pressures and temperatures. *Inorg. Chem*. **2018**, *57*, 6447-6455.

[36] Li, Y.; Zou, Y.; Chen, T.; Wang, X.; Qi, X.; Chen, H.; Du, J.; Li, B. P-V-T equation of state and high-pressure behavior of CaCO3 aragonite. *Amer. Mineral*. **2015**, *100*, 2323-2329.

[37] Xiong, Z.; Liu, X.; Shieh, S.R.; Wang, S.; Chang, L.; Tang, J.; Hong, X.; Zhang, Z.;Wang, H. Some thermodynamic properties of larnite (β-Ca_2SiO_4) constrained by T/P experiment and/or theoretical simulation. *Amer. Mineral*. **2016**, *101*, 277-288.

[38] R.M. Weston, P.S. Rogers. Anisotropic thermal expansion characteristics of wollastonite. Mineralogical Magazine, 1976, 40, 649-651.

[39] J.A. Dalton, D.C. Presnall (1998) The continuum of primary carbonatitic-kimberlitic melt compositions in equilibrium with lherzolite: Data from the system CaO-MgO-Al2O3-SiO2-CO2 at 6 GPa. J. Petrol. 39, 1953.

[40] S. Keshav, H.G. Gudmundur, D. Presnall (2011) Melting phase relations of simplified carbonated peridotite at 12-26 GPa in the systems CaO-MgO-SiO2-CO2

and CaO-MgO-Al2O3-SiO2-CO2: Highly calcic magmas in the transition zone of the Earth. J. Petrol. 52, 2265.

[41] K.D. Litasov, E. Othani (2009) Solidus and phase relations of carbonated peridotite in the system CaO-Al2O3-MgO-SiO2-Na2O-CO2 to the lower mantle depths. Phys. Earth Planet. Int. 177, 46.

[42] S. Ghosh, E. Othani, K.D. Litasov, H. Terasaki (2009) Solidus of carbonated peridotite from 10 to 20 GPa and origin of magnesiocarbonatite melt in the Earth's deep mantle. Chem. Geol. 262, 17.

[43] Santamaria-Perez, D.; Mukherjee, G.D.; Schwager, B.; Boehler, R. High-pressure melting curve of helium and neon: Deviations from corresponding states theory. *Phys. Rev. B*, **2010**, *85*, 214101.

[44] Klotz, S.; Chervin, J.C.; Munsch, P.; Le Marchand, G. *J. Phys. D: Appl. Phys.* **2009**, *42*, 075413.

[45] Mao, K.K.; Xu, J.; Bell, P.M. Calibration of the Ruby Pressure Gauge to 800-Kbar under Quasi-Hydrostatic Conditions. *J. Geophys. Res.-Solid Earth Planets*, **1986**, *91*, 4673–4676.

[46] Hemley, R.J.; Zha, C.S.; Jephcoat, A.P.; Mao, H.K.; Finger, L.W. X-Ray Diffraction and Equation of State of Solid Neon to 110 GPa. *Phys. Rev. B*, **1989**, *39*, 11820-11827.

[47] Cazorla, C.; MacLeod, S.G.; Errandonea, D.; Munro, K.A.; McMahon, M.I.; Popescu, C. Thallium under extreme compression. *J. Phys.: Condens. Matter*, **2016**, *28*, 445401.

[48] Dorogokupets, P.I.; Dewaele, A. Equations of state of MgO, Au, Pt, NaCl-B1, and NaCl-B2: Internally consistent high-temperature pressure scales. *High Press. Res.*, **2007**, *27*, 431-446.

[49] Fauth, F.; Peral, I.; Popescu, C.; Knapp, M. The new material science powder diffraction beamline at ALBA synchrotron. *Powder Diffraction.*, **2013**, *28*, 5360-5370.

[50] Prescher, C.; Prakapenka, V.B. DIOPTAS: A Program for Reduction of Two-Dimensional X-Ray Diffraction Data and Data Exploration. *High Press. Res*., **2015**, *35*, 223−230.

[51] J. Laugier, B. Bochu, LMGP-Suite Suite of Programs for the interpretation of Xray Experiments, ENSP/Laboratoire des Matériaux et du Génie Physique, France, <http://www.inpg.fr/LMGP> and <http://www.ccp14.ac.uk/tutorial/lmgp/>.

[52] Holland, T.J.B.; Redfern, S.A.T. Unit cell refinement from powder diffraction data: the use of regression diagnostics". *Mineral. Magaz., **1997**, 61*, 65-77.

[53] Nolze, G.; Kraus, W. Powdercell 2.0 for Windows. *Powder Diffraction*, **1998**, *13*, 256−259.

[54] Agilent, CRYSALIS^{Pro} software system, version 1.171.36.28, Agilent Technologies UK Ltd., Oxford, UK, **2013**.

[55] L. J. Farrugia, J. Appl. Cryst. **2012**, *45*, 849-854.

[56] Kresse, G.; Furthmuller, J. Efficiency of ab-initio total energy calculations for metals and semiconductors using a plane-wave basis set. Comput. *Mater. Sci.* **1996**, *6*, 15–50

[57] Kresse, G.; Hafner, J. Ab-Initio molecular-dynamics simulation of the liquid-metal amorphous-semiconductor transition in germanium. *Phys. Rev. B* **1994**, *49*, 14251–14269

[58] Kresse, G.; Hafner, J. Ab initio molecular-dynamics for liquid-metals. *Phys. Rev. B* **1993**, *47*, 558–561.

[59] Hohenberg, P.; Kohn, W. Inhomogeneous Electron Gas. *Phys. Rev.* **1964**, *136*, 864−871.

[60] Perdew, J.P.; Ruzsinszky, A.; Csonka, G.I.; Vydrow, O.A.; Scuseria, G.E.; Constantin, L.A.; Zhou, X.; Burke, K. Restoring the density-gradient expansion for exchange in solids and surfaces. *Phys. Rev. Lett*. **2008**, *100*, 136406.

[61] Blöchl, P.E. Projector augmented-wave method. *Phys. Rev. B* **1994**, *50*, 17953–17979

[62] Kresse, G.; Joubert, D. From ultrasoft pseudopotentials to the projector augmented-wave method. *Phys. Rev. B* **1999**, *59*, 1758–1775.

[63] Monkhorst, H.J.; Pack, J.D. Special points for Brillouin-zone integrations. *Phys. Rev. B* **1976**, *13*, 5188–5192.

[64] Mujica, A.; Rubio, A.; Munoz, A.; Needs, R.J. High-pressure phases of group-IV, III-V, and II-VI compounds. *Rev. Mod. Phys.* **2013**, *75*, 863–912.

Acknowledgements

We are thankful for the financial support received from the Spanish Ministry of Economy and Competitiveness through national projects MAT2016-75586-C4-3-P and MAT2015-71070-REDC (MALTA Consolider). D.S-P, J.R-F, and T. M acknowledge financial support of the Spanish MINECO for the RyC-2014-15643 Ramón y Cajal Grant, the IJCI-2014-20513 Juan de la Cierva Fellowship and a FPI Fellowship, respectively. R. Ch-J. acknowledges the European Union Horizon 2020 Program for the Marie Sklodowska-Curie grant Nr. 704998. The Generalitat Valenciana is also acknowledged for financial support (project BEST-2018/203). Authors thank PETRA III and ALBA-CELLS synchrotrons for providing beamtime. British Crown Owned Copyright 2018/AWE. Published with permission of the Controller of Her Britannic Majesty's Stationery Office.

Author contributions

D.S.P. proposed the research and did the project planning. D.S.P., J.R.F, T.M., V.G.C., S.M., and C.P. performed the X-ray diffraction measurements in three different synchrotron beamtimes at PETRA III and ALBA-CELLS. Diffraction data were later analyzed by D.S.P., J.R.F and R.Ch.J. The Raman spectroscopy measurements and analysis were carried out by D.S.P., M.P.A. and E.G. The *ab initio* calculations were done by P. R.H. and A.M. The writing of the manuscript was done by D.S.P., and all the authors contributed to revising it.

Table 1.- Experimental details of the $Ca_5(Si_2O_7)(CO_3)_2$ post-tilleyite single-crystal structure refinements at 10.8 GPa

Crystal data	
Chemical formula	$Ca_5(Si_2O_7)(CO_3)_2$
Crystal system	Monoclinic
Space group	$P2_1$
Unit cell parameters	a = 7.3402(11) Å
	b = 9.7652(7) Å
	c = 14.354(9) Å
	β = 103.88(4)º
Cell volume	998.8(9) Å^3
Z	4
Density	3.25 g/cm^3
Crystal structure refinement	
Total number of reflections	6377
Unique reflections	5205
Nº. refl. I > 3σ(I)	4355
R_{int}	0.0578
R1	0.0553
$R1_{all}$	0.0672
wR2	0.1355
Nº. parameters	178
GooF	0.981

Table 2.- Atomic coordinates and isotropic displacements (U_{iso}) of $Ca_5(Si_2O_7)(CO_3)_2$ post-tilleyite phase at 10.8 GPa.

Atom	x	y	z	U_{iso}
Ca1	0.3197(2)	0.11533(14)	0.4325(2)	0.0103(2)
Ca2	0.1669(2)	0.60264(14)	0.5757(2)	0.0104(2)
Ca3	0.7990(2)	0.35788(14)	0.8650(3)	0.0123(3)
Ca4	0.32962(19)	0.37492(13)	0.8588(2)	0.0105(2)
Ca5	0.18118(19)	0.22126(13)	0.6343(2)	0.0098(2)
Ca6	0.9917(2)	0.81712(15)	0.7512(3)	0.0120(2)
Ca7	0.3427(2)	0.01681(14)	0.9344(2)	0.0116(2)
Ca8	0.33798(19)	0.74761(14)	0.3808(2)	0.0104(2)
Ca9	0.17152(19)	0.47862(14)	0.0473(2)	0.0098(2)
Ca10	0.5049(2)	0.32289(15)	0.2506(2)	0.0116(2)
Si1	0.8222(3)	0.39301(19)	0.4558(3)	0.0080(3)
Si2	0.1194(3)	0.19132(19)	0.0452(3)	0.0083(3)
Si3	0.6873(3)	0.2176(2)	0.0487(3)	0.0083(3)
Si4	0.3823(3)	0.40791(19)	0.4538(3)	0.0080(3)
C1	0.4829(9)	0.6123(6)	0.2392(11)	0.0091(10)
C2	0.0517(9)	0.5120(6)	0.7340(11)	0.0100(10)
C3	0.4380(9)	0.0276(6)	0.2744(11)	0.0099(10)
C4	0.0225(10)	0.1234(6)	0.7899(12)	0.0106(10)
O1	0.0383(9)	0.4955(6)	0.8220(11)	0.0169(11)
O2	0.9651(7)	0.6079(5)	0.6802(9)	0.0112(8)
O3	0.5793(8)	0.3194(6)	0.9685(9)	0.0141(10)
O4	0.2899(7)	0.3394(5)	0.3533(9)	0.0113(9)
O5	0.1753(9)	0.2761(6)	0.9601(11)	0.0207(12)
O6	0.9762(10)	0.0206(7)	0.8306(11)	0.0247(14)
O7	0.6201(7)	0.0628(5)	0.0379(9)	0.0111(9)
O8	0.8894(7)	0.2128(6)	0.0165(9)	0.0119(9)
O9	0.8125(8)	0.3297(6)	0.3525(10)	0.0141(10)
O10	0.6115(7)	0.3952(5)	0.4787(9)	0.0116(9)
O11	0.1398(7)	0.0303(5)	0.0292(9)	0.0113(9)
O12	0.9159(7)	0.2865(5)	0.5385(9)	0.0115(9)
O13	0.3464(7)	0.5647(5)	0.4714(9)	0.0116(9)
O14	0.5296(7)	0.1194(5)	0.3309(9)	0.0114(9)
O15	0.8930(7)	0.5467(5)	0.4733(9)	0.0117(9)
O16	0.4528(8)	0.0172(6)	0.1873(9)	0.0145(10)
O17	0.3460(7)	0.3062(5)	0.5369(9)	0.0103(8)
O18	0.4366(8)	0.5356(6)	0.1639(9)	0.0151(10)
O19	0.5385(8)	0.5618(6)	0.3222(10)	0.0145(10)
O20	0.4781(8)	0.7431(6)	0.2324(10)	0.0158(10)
O21	0.3238(7)	0.9526(5)	0.3059(9)	0.0108(8)
O22	0.7111(8)	0.2953(5)	0.1487(10)	0.0139(10)
O23	0.1668(8)	0.4378(5)	0.7001(9)	0.0130(9)
O24	0.2063(8)	0.2685(6)	0.1446(10)	0.0140(10)
O25	0.9075(9)	0.2151(7)	0.7500(11)	0.0253(14)
O26	0.1988(9)	0.1394(6)	0.7916(12)	0.0217(13)

Figure captions

Figure 1.- Structures of $Ca_5(Si_2O_7)(CO_3)_2$ tilleyite (top) and high-pressure post-tilleyite (bottom) projected along the three unitcell axes. Blue, light gray, light green and red spheres represent C, Si, Ca and O atoms, respectively. Cell edges are depicted as solid black lines. Red solid lines on post-tilleyite projections demarcate the location of tilleyite unitcell contents, for the sake of comparison between structures.

Figure 2.- Pressure dependence of the lattice parameters of tilleyite and post-tilleyite $Ca_5(Si_2O_7)(CO_3)_2$ phases. Black squares, circles and triangles denote the *a*, *b* and *c* axes of both structure-types. Blue squares show the evolution of the monoclinic β angle with pressure. Solid and empty symbols correspond to the initial $P2_1/n$ tilleyite and the high-pressure $P2_1$ post-tilleyite phases. Experimental fits are depicted as solid and dashed black and blue lines. Results from DFT calculations are represented with red lines.

Figure 3.- Pressure dependence of the unit-cell volume of $Ca_5(Si_2O_7)(CO_3)_2$ tilleyite. Solid squares correspond to powder XRD data, and empty blue triangles and green circles correspond to single-crystal XRD data. Fits to all the experimental results for the low- and high-pressure phases are depicted as solid and dashed black lines, respectively. Results from DFT calculations are represented with red lines.

Figure 4.- Selected room-temperature Raman spectra of powder $Ca_5(Si_2O_7)(CO_3)_2$. Intensity scales vary from spectral regions and it has been adapted for clarity as indicated in the top left side of each panel. Black is used for tilleyite, green for post-tilleyite and brown for higher pressure phase. δ symbols denote bending modes and ν stretching modes, respectively.

Figure 5.- Internal energy as a function of volume per unitcell for the initial $P2_1/n$ tilleyite and the $P2_1$ post-tilleyite phases. The enthalpy variation *versus* pressure curve for both polymorphs is depicted in the inset (taking the $P2_1/n$ tilleyite structure as reference).

Figure 6.- Representation of the evolution under compression of polyhedral unit volumes.

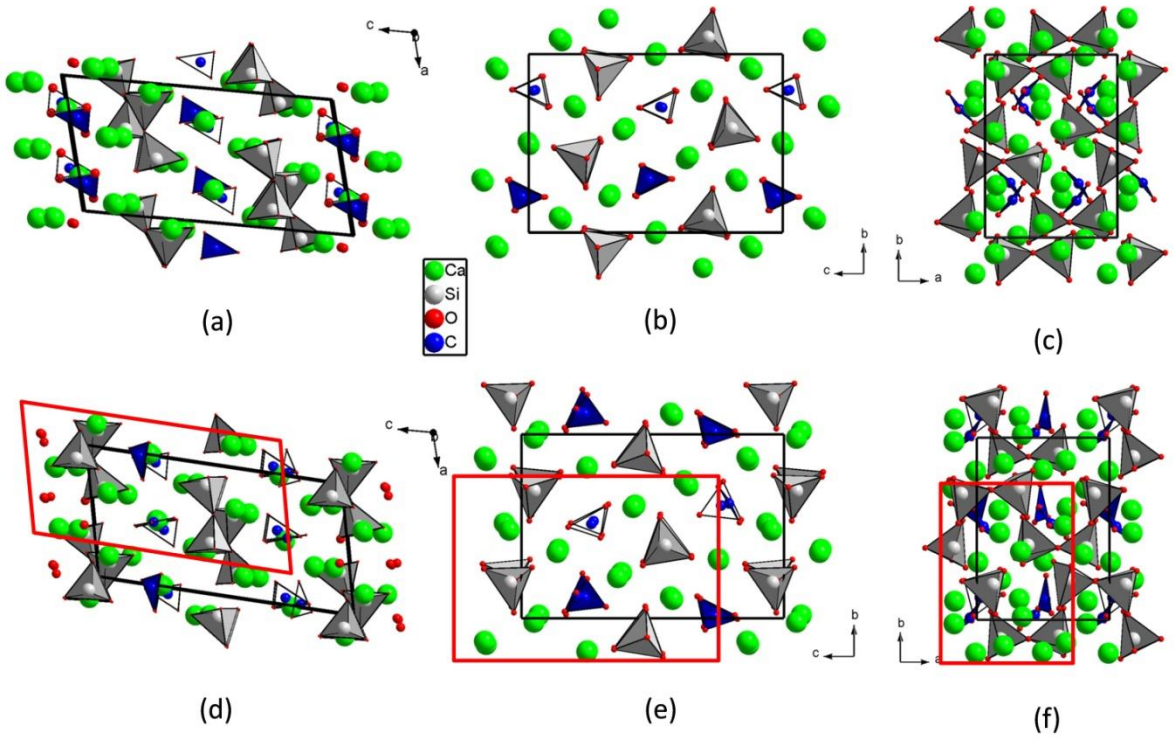

Figure 1

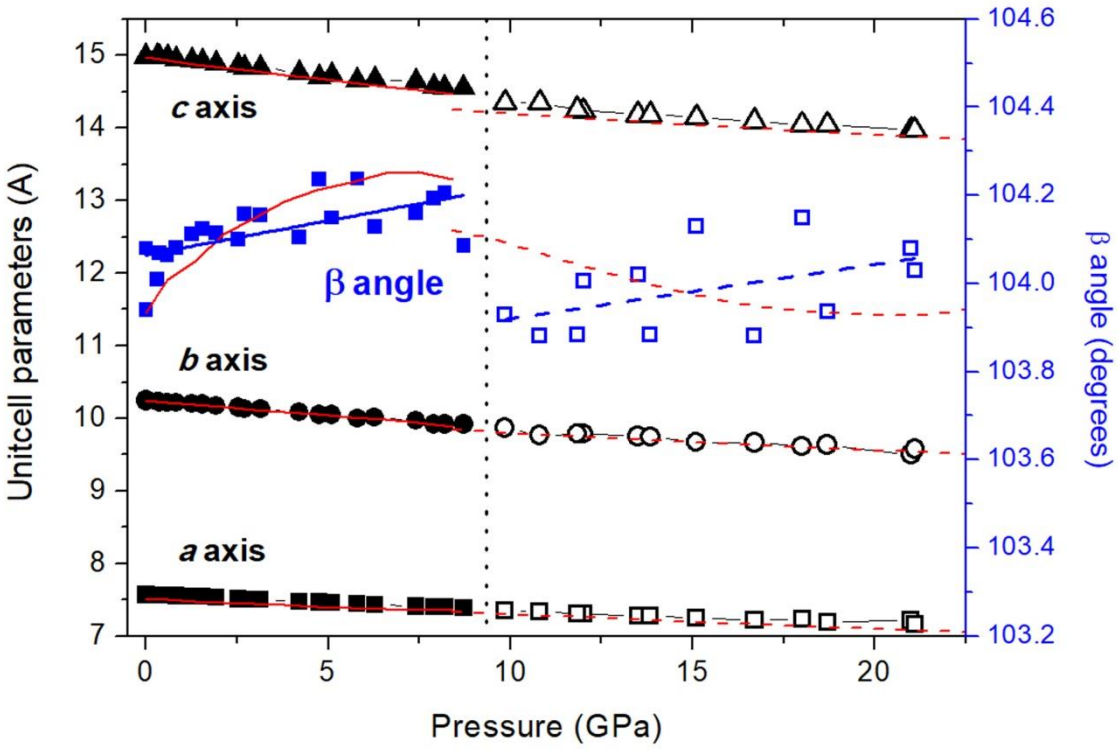
Unitcell parameters (A)
β angle (degrees)
Pressure (GPa)
c axis
β angle
b axis
a axis
15
14
13
12
11
10
9
8
7
0
5
10
15
20
104.6
104.4
104.2
104.0
103.8
103.6
103.4
103.2

Figure 2

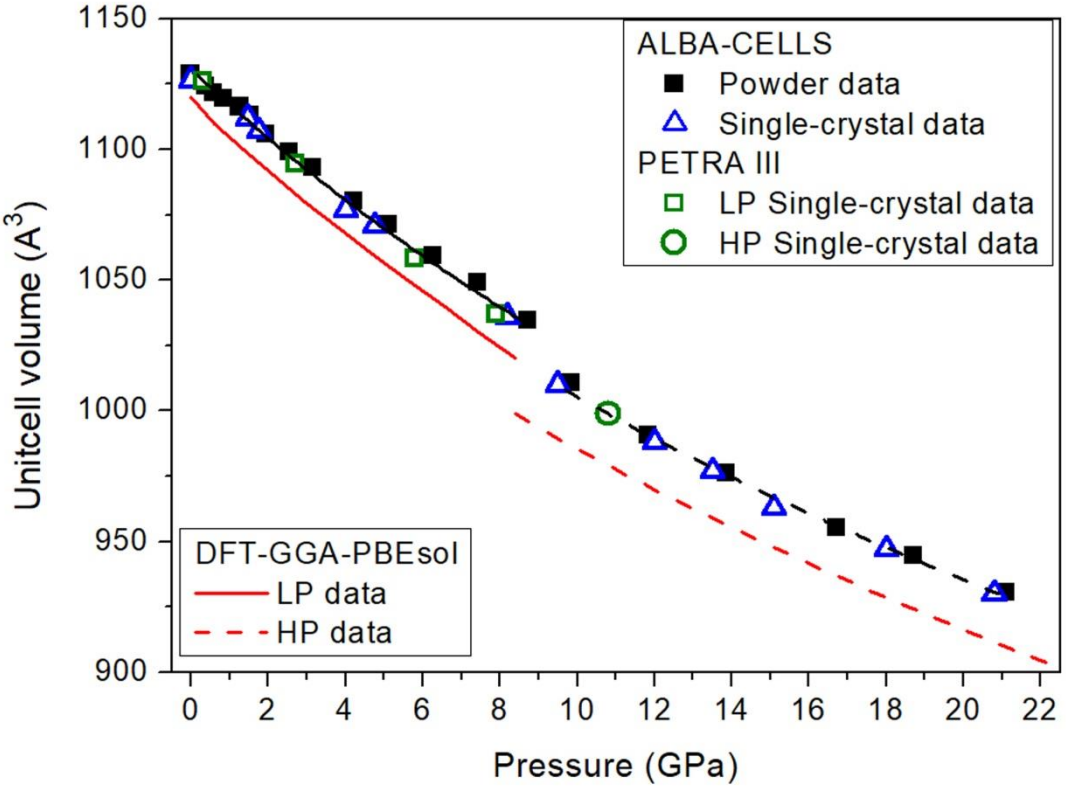
ALBA-CELLS
Powder data
Single-crystal data
PETRA III
LP Single-crystal data
HP Single-crystal data
DFT-GGA-PBEsol
LP data
HP data
Unitcell volume (A3)
Pressure (GPa)
1150
1100
1050
1000
950
900
0
2
4
6
8
10
12
14
16
18
20
22

Figure 3

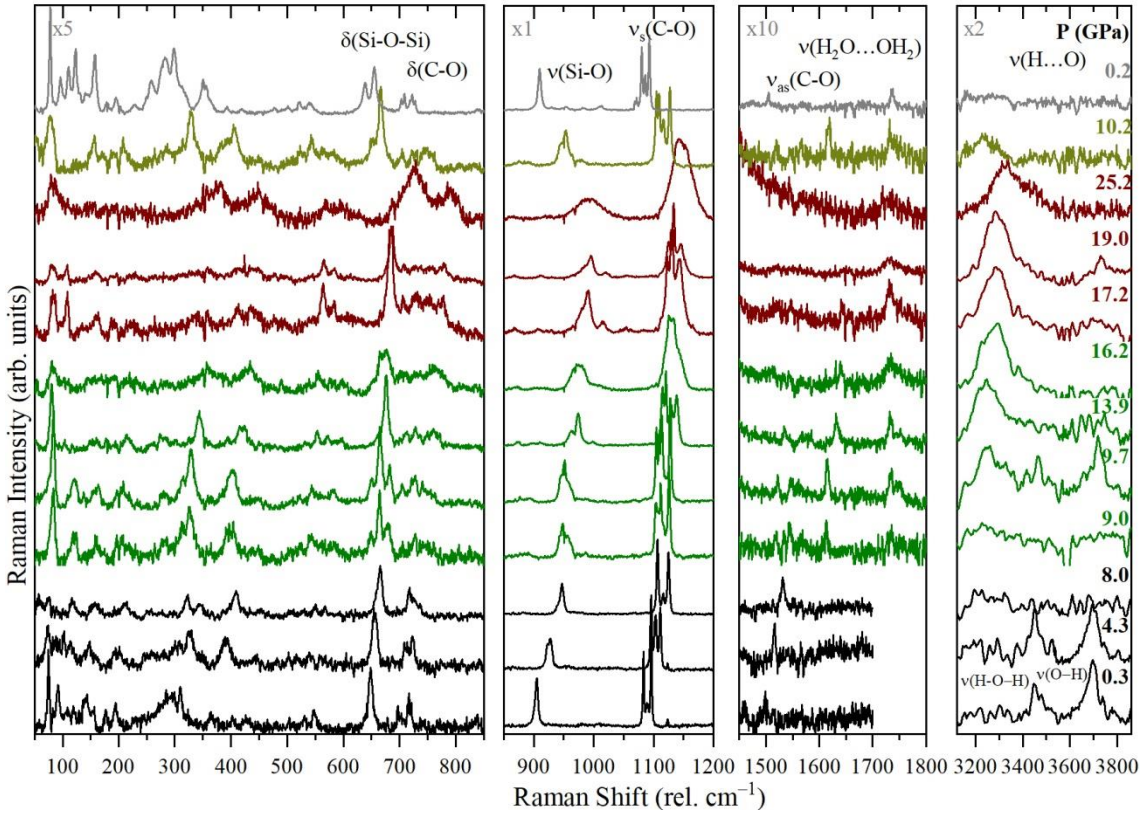
x5
δ(Si-O-Si)
δ(C-O)
x1
ν(Si-O)
ν_s(C-O)
x10
ν(H$_2$O…OH$_2$)
ν_{as}(C-O)
x2
P (GPa)
ν(H…O)
0.2
10.2
25.2
19.0
17.2
16.2
13.9
9.7
9.0
8.0
4.3
0.3
ν(H-O-H)
ν(O–H)
Raman Intensity (arb. units)
100 200 300 400 500 600 700 800
900 1000 1100 1200
1500 1600 1700 1800
3200 3400 3600 3800
Raman Shift (rel. cm^{-1})

Figure 4.

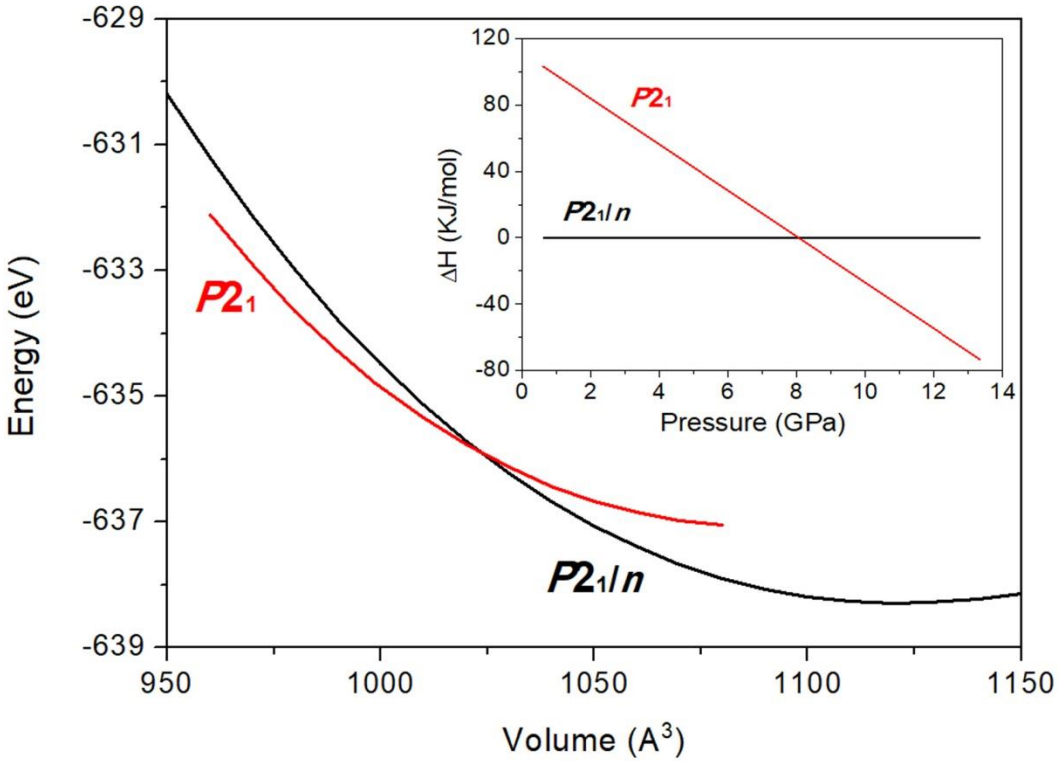
Energy (eV)
-629
-631
-633
-635
-637
-639
950
1000
1050
1100
1150
Volume (A3)
P21
P21/n
ΔH (KJ/mol)
120
80
40
0
-40
-80
0
2
4
6
8
10
12
14
Pressure (GPa)
P21
P21/n

Figure 5

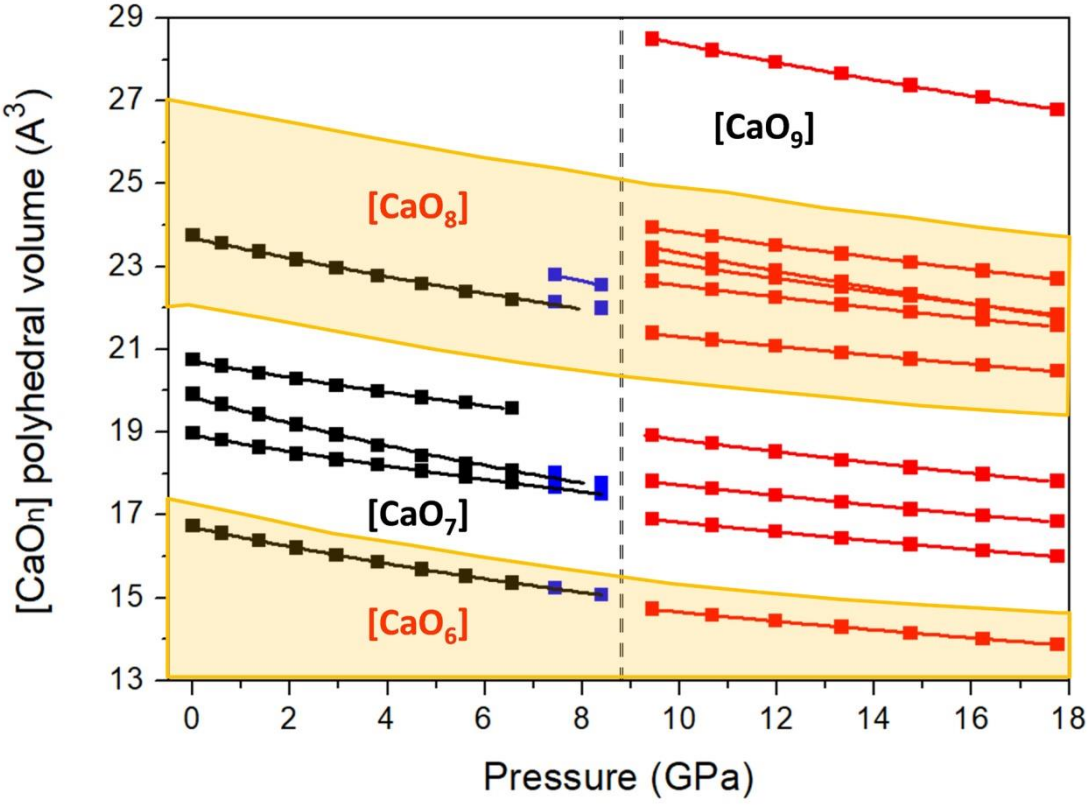
[CaO9]
[CaO8]
[CaO7]
[CaO6]
[CaOn] polyhedral volume (A3)
Pressure (GPa)
29
27
25
23
21
19
17
15
13
0
2
4
6
8
10
12
14
16
18

Figure 6

SUPPLEMENTARY MATERIAL

Table 1a.- Experimental details of tilleyite single-crystal refinement at ambient conditions (Our data).

Table 1b.- Atomic coordinates of tilleyite at ambient conditions (Our data).

Table 2.- Atomic coordinates of tilleyite at ambient conditions from Grice 2005 in the setting P21/n, for the sake of comparison.

Figure 1.- LeBail of an XRD powder pattern.

Cifs.- (Experimental data) RP, 7.9 GPa and 10.8 GPa. (Theor. data) 10.8 GPa

Table 3a.- Experimental details of tilleyite single-crystal refinement at 7.9 GPa.

Table 3b.- Atomic coordinates of tilleyite at 7.9 GPa.

Table 4.- Lattice parameters of the low-pressure phase (all the powder and single crystal experiments)

Table 5.- Lattice parameters of the high-pressure phase (all the powder and single crystal experiments)

Figure 2.- Experimental and theoretical pressure dependence of the Raman-mode frequencies of $Ca_5(Si_2O_7)(CO_3)_2$ up to 19 GPa.

Figure 3a.- Calculated evolution of the Raman modes of tilleyite

Figure 3b.- Calculated evolution of the IR modes of tilleyite

Figure 4.- Calculated evolution of the Raman and IR modes of post-tilleyite

Table 6.- Polyhedral compressibilities.